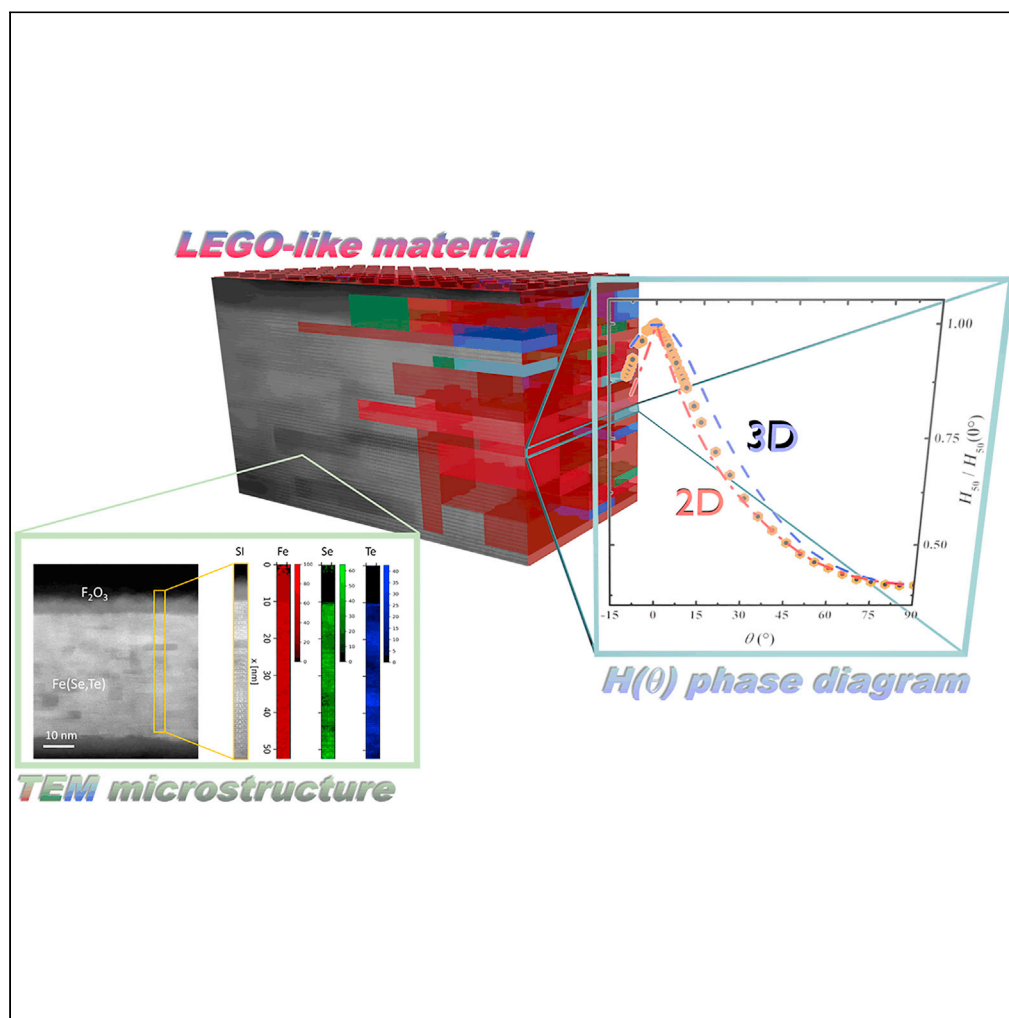**Article**

Unveiling intrinsic material and extrinsic pinning dimensionality in superconductors: Why Fe(Se,Te) is able to mimic YBCO

Gaia Grimaldi, Masood R. Khan, Antonio Leo, ..., Massimiliano Polichetti, Angela Nigro, Valeria Braccini

gaia.grimaldi@spin.cnr.it (G.G.)
mario.scudeiri@imm.cnr.it (M.S.)

Highlights

A general method to reveal material dimensionality and pinning anisotropy at once

Iron-based Fe(Se,Te) film on CaF_2 is able to mimic YBCO layered superconductor

H-θ phase diagram and TEM show 2D Lego-block features in Fe(Se,Te) superconductor

Article

Unveiling intrinsic material and extrinsic pinning dimensionality in superconductors: Why Fe(Se,Te) is able to mimic YBCO

Gaia Grimaldi,[1,6,*] Masood R. Khan,[1,2] Antonio Leo,[1] Mario Scuderi,[3,*] Francesco Rizzo,[4] Andrea Augieri,[4] Giuseppe Celentano,[4] Armando Galluzzi,[1,2] Michela Iebole,[5] Massimiliano Polichetti,[1,2] Angela Nigro,[1,2] and Valeria Braccini[5]

SUMMARY

Discovery of iron-based superconductors paved the way to a competitor of high-temperature superconductors, easier to produce, better performing in high fields, and promising to be less expensive. Critical parameters are investigated by resistivity measurements as a function of temperature, field, and angle $R(T,H,\theta)$. This work presents a deep analysis of H-θ phase diagram of PLD-processed Fe(Se,Te) superconducting films, thus revealing material and pinning anisotropy at once. By selecting different thresholds along the $R(T,H,\theta)$ curves, all possible regimes emerge. Surprisingly, anisotropy arises moving from the upper critical field toward the irreversibility line: gradually a non-monotonous transition from 3D to 2D, and backward to 3D occurs. Although Fe(Se,Te) appears as a 3D superconductor, its anisotropic pinning landscape shows up similarities with an intrinsic layered superconductor and Fe(Se,Te) definitely mimics YBCO. We propose a general method to disentangle, in any other superconductor, material dimensionality and pinning anisotropy that are key constraints for applications.

INTRODUCTION

A lot of interest has been grown recently on iron-based superconductors (IBSs), which is reminiscent of the widespread research on high-temperature cuprate superconductors (HTSs). Low anisotropy and high critical fields imply that these IBS materials are promising for applications,[1,2] and competitors with the well-known HTS cuprates.[3] The Fe(Se,Te) has the lowest anisotropy of all the IBS families, the simplest crystallographic structure, and no toxic components, making it more attractive than other IBSs. Moreover, the Fe(Se,Te) can be considered as model material for low anisotropic superconductors interesting for high field applications. Therefore, it is relevant to study the upper critical field in order to understand the mechanism of superconductivity in Fe(Se,Te), as it has been done on YBCO. However, in all the HTS, the study of vortex dynamics and pinning properties outlines the complexity and the interlocked behavior between the anisotropic nature of the compound with the anisotropy induced by material defects.[4–7] Indeed, the critical fields are crucial superconducting parameters because they provide valuable information about fundamental superconducting properties such as coherence length, anisotropies, details of underlying electronic structures, as well as insights into the pair-breaking mechanism.[8] Nonetheless, the depairing current is linked to the upper critical field but the critical current density is associated with the irreversibility field, which is an essential property for applications.[9–11]

In general, the high critical temperature T_c of the HTS materials leads to an extended region of thermally activated flux flow, and the complicated physics of anisotropic pinning and vortex lattice dynamics make it difficult to obtain H_{c2} from $R(T)$ measurements in a reliable manner when the chosen criterion other than the 90% R_N is used.

In order to estimate the upper critical field, different measurement techniques such as thermal conductivity,[12,13] specific heat,[14–16] and electrical transport measurements[17–21] are commonly used, besides magnetic measurements.[22] Although electrical transport measurements are usually employed to estimate the upper critical field, H_{c2}, the selection of the appropriate criterion is crucial to this aim. Indeed, varying this criterion corresponds to looking at different regions along the resistive transition, i.e., different regimes where different mechanisms can take place. Such an R_x threshold is generally expressed as a percentage, x, of the normal state resistance, R_N, in resistivity measurements. The more actively used is the 90% of normal state resistance, R_{90}, to estimate the upper critical field. However, it is not unusual for H_{c2} to be determined by using the 50% of the R_N value (R_{50}) and this is commonly applied to any superconducting material.[23–26] The temperature at the 50%

of the R_N is indeed associated with the mean-field critical temperature.[27,28] We note that, in literature, materials exist for which such a criterion choice becomes significant, prompting our investigation.

On top of that, the upper critical fields of layered superconductors are anisotropic and deviations from the anisotropic Ginzburg-Landau theory can be expected due to the anisotropy of the superconducting gap like in the HTS, as well in multiband materials as the IBS, or in 2D and 1D nanostructured superconductors.

In this work, we explore the different regimes along the resistive transition by choosing several thresholds to determine the critical fields and looking to the resulting angular dependence $H_{c2}(\theta)$ and $H_{irr}(\theta)$ in Fe(Se,Te) and YBCO materials. Our findings highlight how $H_{c2}(\theta)$ changes by changing the threshold from the 90% to the 50% of R_N; this can be interpreted as a different structural and pinning influence on determining the H-θ phase diagram. Particularly for Fe(Se,Te), a totally unexpected trend of $H_{c2}(\theta)$ anisotropy is observed: it starts from a 3D behavior at R_{90} and reaches at R_{50} an almost 2D behavior in the whole angular range. A similar trend is observed for YBCO, that is expected to start with a 3D anisotropic behavior of $H_{c2}(\theta)$, but then it achieves a 2D behavior at R_{50}. Furthermore, at R_{10}, a significant difference emerges due to the fact that for Fe(Se,Te) an isotropic pinning is expected owing to the very low anisotropy γ_J around 1 as deduced from the critical current density ratio[4] $J_c^{\parallel}/J_c^{\perp}$, whereas in YBCO the layered structure is still able to act as a stronger pinning preserving the anisotropic 2D behavior down to R_{10}.

By the comparison between these two materials, we are able to identify the layered structure and pinning influence that play a concurrent dominant role in determining the angular dependence in the H-θ phase diagram. Finally, we demonstrate how the Fe(Se,Te) material can mimic the YBCO through an insight into material defects by high-resolution transmission electron microscopy. The complex microstructure observed in the film is characterized by a prevalent defect orientation along the *ab*-plane. It also contains distinct domains with varying stoichiometry that form a layered film, which confers a 2D character to the material. This explains the observed pinning mechanism in Fe(Se,Te), which is similar to that usually found in the intrinsic layered YBCO structure. Our method of studying the H-θ phase diagram will provide a general approach to any other unknown superconductor, thus unveiling material dimensionality and pinning anisotropy.

RESULTS

The investigated Fe(Se,Te) thin films of about 100 nm thickness were grown on [001] CaF$_2$ substrates in a high vacuum pulsed laser deposition (PLD) system equipped with a Nd:YAG laser at 1,024 nm. The FeSe$_{0.5}$Te$_{0.5}$ PLD target was synthesized with a two-step method.[29] The optimized laser parameters to obtain high-quality epitaxial 11 thin films were 3 Hz repetition rate, 2 J/cm^2 laser fluency (2 mm^2 spot size), and 5 cm distance between target and sample. The deposition was carried out at a pressure of 10^{-8} mbar, while the substrate was kept at 350°C. The standard high quality of the films is confirmed by X-ray diffraction analysis, showing only the (00l) reflections of the films and substrates in the θ-2θ scans, indicating the excellent purity of the phase and the optimum *c*-axis alignment of the growth. Omega scans on these reflections show rocking curves having a full width at half maximum of the order of 1°. φ scans indicated that the films grow rotated by 45° with respect to the *a*-axis of 5.4620 Å due to the good matching with half the diagonal[30] a/√2 = 3.862 Å.

YBCO thin films on STO substrates are also routinely produced by PLD.[31] A 16T cryogen-free magnet (CFM16T) system by Cryogenic Ltd. was used to perform the magnetoresistance measurements. Details are described in our previous works.[5,19,32] To determine the angular dependence of the upper critical field, the sample was mounted on a double-axis rotating platform in the CFM16T. The sample rotation has been performed by keeping the maximum Lorentz force configuration. The θ rotation angle is the angle formed by H and the sample's crystallographic structure: a rotation angle of $\theta = 0°$ corresponds to H parallel to *ab*-planes, whereas a rotation angle of $\theta = 90°$ corresponds to H parallel to the *c*-axis. The microstructure and elemental composition of the Fe(Se,Te) thin film were investigated by transmission electron microscopy (TEM). The Fe(Se,Te) thin film was removed from the CaF$_2$ substrate by means of a mechanical lift-off process, therefore a conventional cross-sectional TEM sample preparation was conducted by preparing a sandwich including the removed film on two expendable substrates. The specimen was subsequently Ar+ ion-milled using a precision ion polishing system by Gatan Inc. with an energy starting from 3 keV, down to a final cleaning energy of 200 eV.

TEM measurements were performed in a probe Cs-corrected JEM-ARM200F by JEOL Ltd., equipped with a cold FEG operated at a primary beam energy of 200 keV in scanning TEM (STEM) mode. An energy filter (GIF Quantum ER) by Gatan Inc. was used for electron energy loss spectroscopy (EELS) measurements.

H-θ phase diagram

We present a comprehensive description on a Fe(Se,Te) sample that can serve as a general reference for other superconducting films. As first, we define the value of R_N as the resistance value at which the transition starts to appear, which is then recognized in the resistance-temperature curve, $R(T)$, as the point at which the experimental data begin to depart from the roughly linear trend (see Figure 1). This gives a value of $R_N = 82\ \Omega$. The irreversibility line $H_{irr}(T)$ and the upper critical field line $H_{c2}(T)$ are frequently estimated in the literature using the criterion $R(T, H_{irr}) = 0.1\ R_N$ and $R(T, H_{c2}) = 0.9\ R_N$, as shown in Figure 1.

Likewise, other authors report on HTS and IBS data of the upper critical fields; in general, the estimation is made by different techniques that strongly support the upper critical field evaluation by electrical transport measurements. For instance, the upper critical field was determined using both specific heat measurement and $R(T, H)$ measurements showing the same trend in the H-T phase diagram.[14,16,33,34] Moreover, Fiamozzi Zignani et al.[35] compared the upper critical field data determined by the calorimetric measurements with the $R(T)$ measurements result of the upper critical field based on the 90% of normal state resistance and they found exactly the same result. However, Tanatar et al.[13] studied the H-T phase diagram of quasi 2D organic superconductor, namely a low-temperature superconductor, through
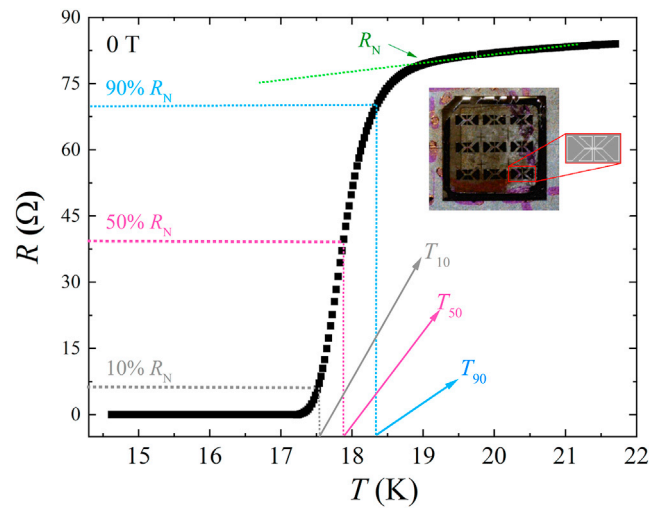
Figure 1. Thresholds selection of resistance as a function of temperature measured with I_{bias} = 100 μA in zero magnetic field on the Fe(Se,Te) microbridge shown in the photographic inset

the thermal conductivity measurements, revealing that the low temperature part of the phase diagram does not match with the mid-point (50% R_N) of the resistive transition.

We estimated the upper critical field from angular measurements and with magnetic field strengths up to 16 T in the Fe(Se,Te) and YBCO thin films. Figure 2 shows the critical fields as a function of the temperature along the *ab*-plane and the *c*-axis as obtained by different xR_N
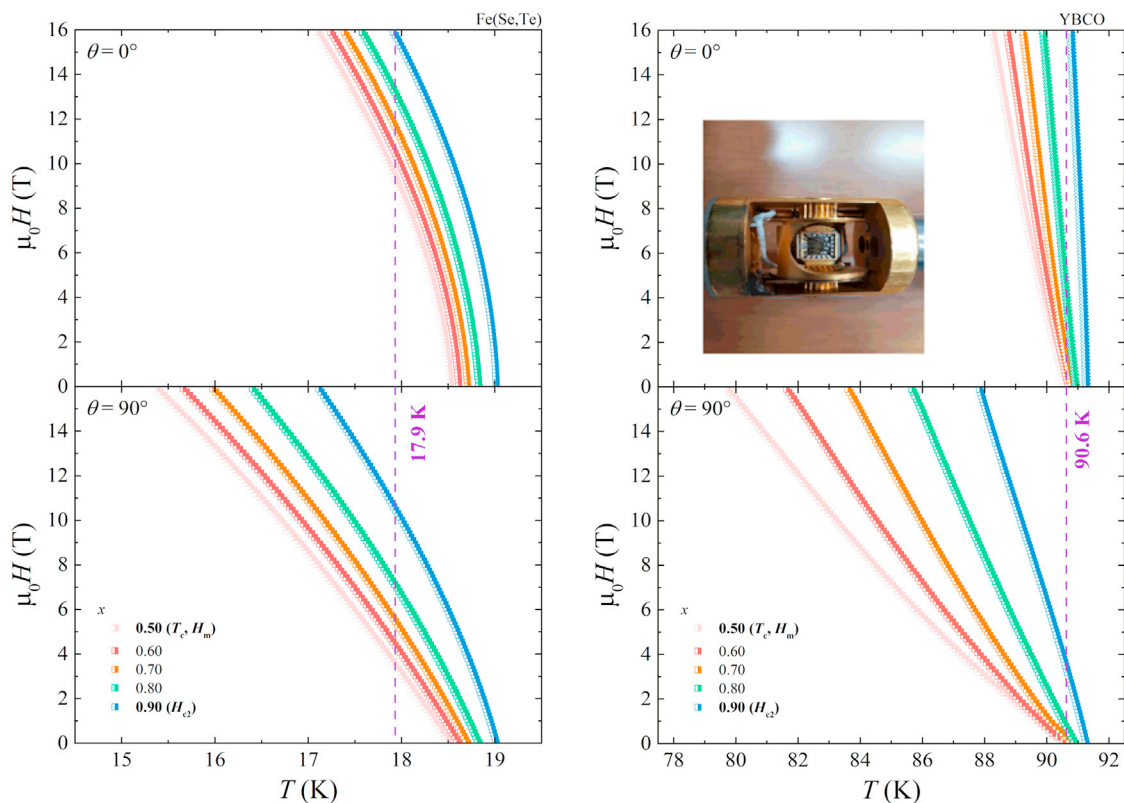

Figure 2. H-T phase diagrams for parallel θ = 0° and perpendicular θ = 90° field orientations (left panel) Fe(Se,Te) sample
(right panel) YBCO sample. In this panel, the YBCO sample mounted on the double-axis rotator platform is also shown.
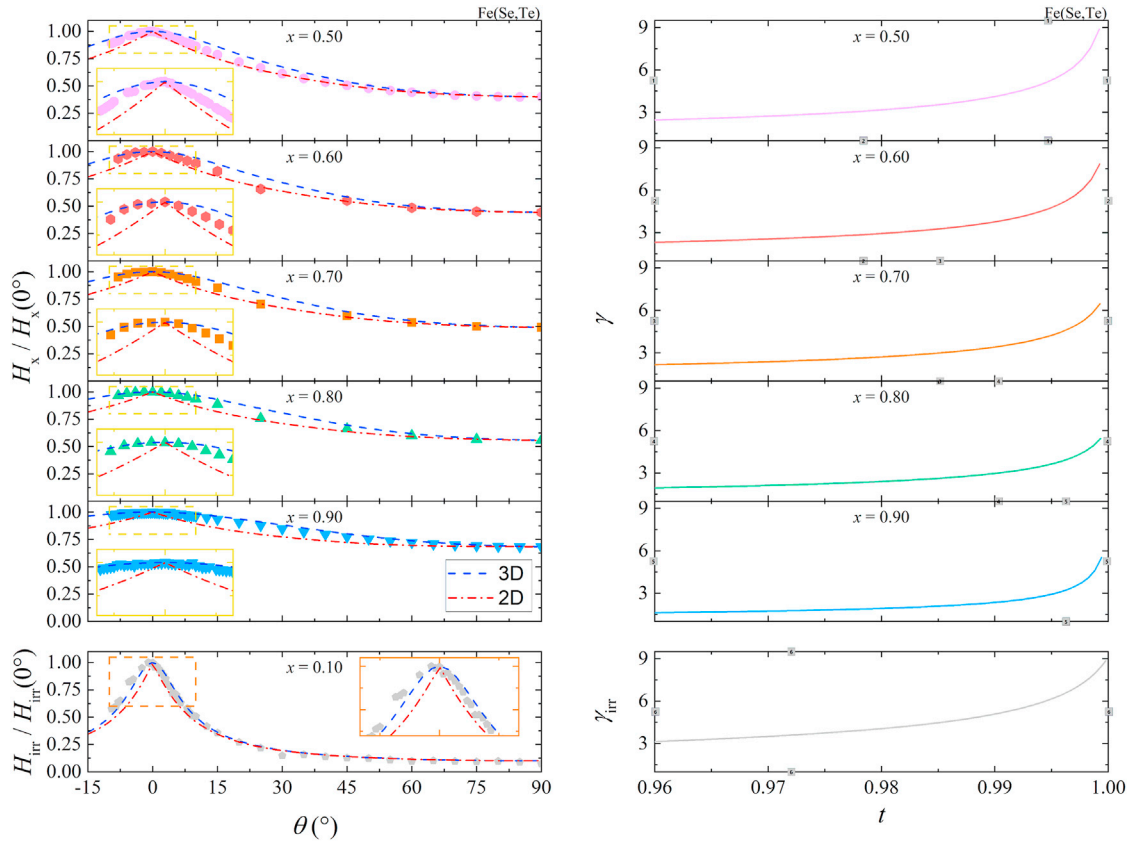
Figure 3. Angular dependence of upper critical field H_{c2} and the anisotropic parameter obtained from transport measurements at different xR_N thresholds, including H_{irr} at $x = 0.1$, for Fe(Se,Te) sample

(left panel) $H_{c2}(\theta)$ at $T = 17.9$ K. (right panel) The anisotropic parameter as a function of normalized temperature $t = T/T_x(H = 0)$.

thresholds obtained by varying x from 90% to 50% of R_N. The different H-θ phase diagrams have been evaluated for angles between $-9.5°$ and $100°$, as we present in the Figure 3 for the Fe(Se,Te) and Figure 4 for YBCO, including $H_{irr}(\theta)$ evaluated at 10% of R_N.

In order to understand the anisotropy behavior of the critical fields, it is instructive to compare the experimental $Hx(\theta)$ behavior with two well-established predictions: the 3D Ginzburg-Landau (GL) and the 2D Tinkham models. The angular dependence of H_{c2} in the 3D GL model is [36]:

$$\left(\frac{H_{c2}(\theta)\sin(\theta)}{H_{c2}^{\perp}}\right)^2 + \left(\frac{H_{c2}(\theta)\cos(\theta)}{H_{c2}^{\parallel}}\right)^2 = 1$$

In this case, $H_{c2}^{\parallel}$ denotes the upper critical field at $\theta = 0°$ and $H_{c2}^{\perp}$ indicates the upper critical field at $\theta = 90°$. The result of the calculation using the GL model is depicted in Figure 3 and in Figure 4, by a blue dashed line that is dome like.

The angular dependence of H_{c2} in 2D superconductors, such as thin films[36] and superlattices,[37] is described by the following equation, which was first derived by Tinkham.

$$\left|\frac{H_{c2}(\theta)\sin(\theta)}{H_{c2}^{\perp}}\right| + \left(\frac{H_{c2}(\theta)\cos(\theta)}{H_{c2}^{\parallel}}\right)^2 = 1$$

The Tinkham model[38] evaluation is depicted in Figures 3 and 4 by a red dashed-dotted line that is cusp like.

In the case of Fe(Se,Te) in Figure 3, by decreasing from 0.9 R_N value down to 0.5 R_N value, the $H_x(\theta)$ curves clearly deviate from a 3D anisotropic material prediction toward a more 2D behavior in the whole angular range. The same trend is observed for the YBCO film in Figure 4. Therefore, the Fe(Se,Te) is mimicking the YBCO at all, despite possessing distinct crystallographic structures.

On the contrary, concerning the $H_{irr}(\theta)$ behavior, the trend is just the opposite: an almost 3D behavior for the Fe(Se,Te) is shown in Figure 3, which corresponds to the much more isotropic pinning found in its critical current (see Figure S1),[4] whereas a dependence closer to 2D is found in Figure 4 for the YBCO owing to at least its intrinsic layered structure that serves as an effective pinning center. It is worth to note that the comparison of experimental $H_{irr}(\theta)$ curves with both predicted curves by 2D Tinkham[38] and 3D GL,[39] respectively, the blue dashed
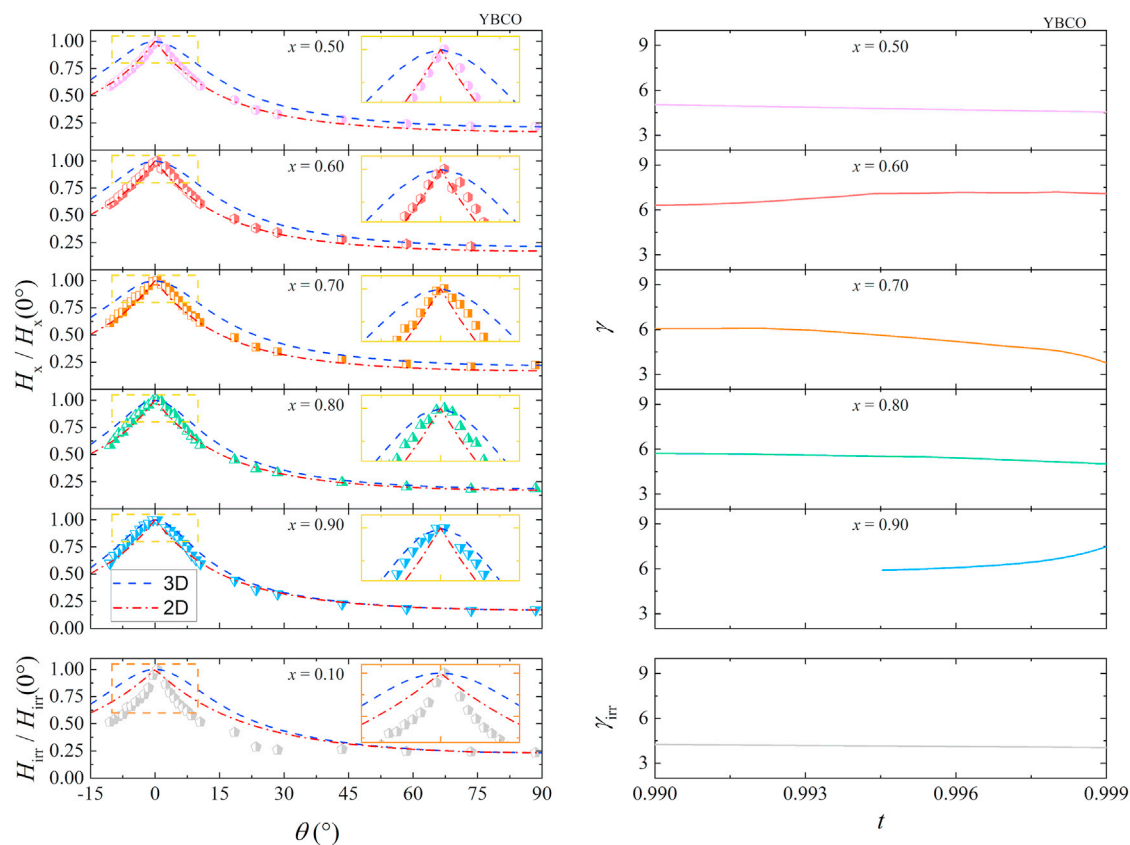
Figure 4. Angular dependence of upper critical field and the anisotropic parameter as a function of normalized temperature for YBCO sample, including H_{irr}

(left panel) $H_{c2}(\theta)$ at $T = 90.6$ K. (right panel) The anisotropic parameter as a function of normalized temperature.

and red dotted lines in Figures 3 and 4, is a first attempt to identify the dimensionality of the pinning mechanism. We are perfectly aware that the two mentioned models usually apply only to determine the dimensionality of material anisotropy.[25–28] Nevertheless, we tried to disentangle intrinsic material anisotropy related to $H_{c2}(\theta)$ from extrinsic pinning anisotropy reflected into $H_{irr}(\theta)$. Indeed, we succeeded on two different materials, Fe(Se,Te) and YBCO, which in principle look like different from both intrinsic structure and pinning properties. Our findings highlight the correct picture on both material and pinning anisotropy in both superconductors.

As a matter of fact, we expect a 3D behavior for the upper critical field of Fe(Se,Te) material due to the estimated anisotropy parameter values that are quite low as a function of both the magnetic field and the temperature.[4] Here, we report an overview of the evaluated parameters according to the various thresholds in Table 1 for the Fe(Se,Te) and in Table 2 for the YBCO; all the $\gamma = H_x(0°)/H_x(90°)$ parameters were found by choosing different xR_N values. In the Tables, we also report the normalization value $T_x(H = 0)$ for the normalized temperatures shown in Figures 3 and 4. H_{max} and H_{min} are the maximum and minimum magnetic field values at 17.9 and 90.6 K for Fe(Se,Te) and YBCO, respectively; field values above 16 T have been extrapolated. For instance, well-known layered materials have very high values of the anisotropy

Table 1. A summary of the evaluated parameters for the different criteria in the Fe(Se,Te) sample: γ(0.96) and γ(0.999) are the values of anisotropic parameter against the normalized temperature 0.96 and 0.999, respectively

x	$T_x(H = 0)$	$T = 17.9$ K		γ(0.96)	γ(0.999)
		H_{max}	H_{min}		
0.5	18.52	9.7	3.7	2.5	8.9
0.6	18.61	10.75	4.6	2.3	7.8
0.7	18.71	11.9	5.7	2.2	6.5
0.8	18.82	13.4	7.3	2.0	5.4
0.9	19.01	16.0	10.7	1.6	5.5

Table 2. A summary of the evaluated parameters for the different criteria in the YBCO sample

| x | $T_x(H = 0)$ | $T = 90.6$ K | | $\gamma(0.995)$ | $\gamma(0.999)$ |
		H_{max}	H_{min}		
0.5	90.63	0.020	0.005	4.7	4.5
0.6	90.70	0.448	0.096	7.1	7.0
0.7	90.79	1.262	0.280	5.5	3.3
0.8	90.92	4.033	0.751	5.5	4.9
0.9	91.27	19.869	3.411	6.0	6.5

parameter and they are expected to exhibit 2D behavior, such as in the case of BiSCCO.[40] Nevertheless, when the anisotropy parameter is comparatively quite small, a similar layered material exhibits 3D behavior as in the case of YBCO.[40] Nonetheless, in Fe(Se,Te) superconductor, as soon as the resistivity threshold was lowered from 90% down to 50%, we observed a 2D anisotropic behavior in our samples. We found that the behavior of γ as a function of temperature strongly changes looking at different regions of the resistive transition. This corresponds to reducing from 90% to 50% of R_N, thus a significant increase of the anisotropic parameter is revealed, at least for the Fe(Se,Te) material (see also Figure 1 in the supplemental information).

Llovo et al.[11] estimated the upper critical field of 122 type iron pnictide superconductor by using different xR_N criteria and anticipated that the upper critical field is unaffected by choosing different criteria. Likewise, in the case of (Ba,K)Fe$_2$As$_2$ superconductor, when the different xR_N criteria are used to estimate the angular behavior of the upper critical field, the results are also unaffected.[41] In addition, Borg et al.[15] revealed that the anisotropic behavior of the upper critical field of FeS single crystal varied slightly when different xR_N criteria for evaluating upper critical field were used.

A possible explanation of the observed 2D behavior in our findings can be related to the pinning properties of the layered-like IBS materials, resembling the YBCO trend. Indeed, the evolution from 3D to 2D is tied to the material layered structure and possibly pinning effects, which are still being debated today in the case of IBS materials. In particular, for the Fe(Se,Te), here we present a much more detailed study on its microstructure to clarify its pinning landscape.

TEM microstructure analysis on Fe(Se,Te)

We employed several methods to study the compositional features of the Fe(Se,Te) sample, combining STEM and EELS. In our previous studies, we focused mostly on the structural properties of the sample, while the chemical composition was investigated only to a limited extent. Specifically, in our recent works,[42,43] the main results were related to the microstructure of the material, revealing *ab* elongated domains interconnected by means of grain boundaries, while the chemical variation was only qualitatively assessed. Here, we used a ternary phase diagram to identify two distinct chemical phases within the sample, which could not be resolved based only on the STEM imaging and EELS elemental mapping alone. In Figure 5, two STEM images and related EELS elemental maps of the sample at a higher magnification are presented. In the two STEM images obtained in low and high magnification, the mass contrast reveals elongated domains along the *ab*-plane, which are consistent with the domains previously discussed in the literature.[42,44] The EELS elemental maps in Figure 5C reveal a constant iron concentration, while selenium and tellurium show a varying composition within the region identified by the spectrum image (SI). This gradual variation is not discernible within the determined phase regions. Only by using the ternary diagram, it is possible to clearly recognize the actual stoichiometry within these regions, since the overlapping of different domains with different stoichiometries does not allow for a direct measurement of the stoichiometry of the individual domain.

By utilizing the ternary diagram, we were able to determine the actual stoichiometry of these domains. In Figure 6, we present a ternary diagram where each data point represents the atomic percentage, measured by EELS, at a specific location in the SI. Each data point is also assigned a color, according to the RGB triangle, based on its position in the ternary diagram. These color-coded data points are grouped in a specific region and form two clusters with slightly different colors, one tending toward green (cluster A) and the other toward red (cluster B). The center of the two clusters represents the average atomic composition of all the points associated to each cluster. By back-mapping these data points to what we call an RGB elemental map, we find that the film is composed of alternating bands with different colorations corresponding to two distinct stoichiometries. This suggests that the Fe(Se,Te) film consists of domains characterized by two distinct stoichiometries. The stoichiometric values of these two phases, which were determined by calculating the centers of the clusters, are FeSe$_{0.7}$Te$_{0.3}$ for cluster A and FeSe$_{0.5}$Te$_{0.5}$ for cluster B. A similar phase separation was induced in a recent study[45] where the authors, in order to enhance the flux pinning behavior of Fe(Se, Te), successfully tuned a phase separation via the addition of FeF$_2$ to the raw materials, resulting in a macroscopically ordered phase separation with well-defined stoichiometry that leads to a higher critical current density and a narrower transition width. We emphasize that the phase separation we observed is totally spontaneous.

DISCUSSION AND CONCLUSIONS

Summarizing, the Fe(Se,Te) on CaF$_2$ is able to mimic the layered structure of YBCO film due to the growth-induced defects in the case of Fe(Se,Te) rather than intrinsic layering of YBCO. Such material defects as elongated grains shaped along the *ab*-plane[42] are sketched in
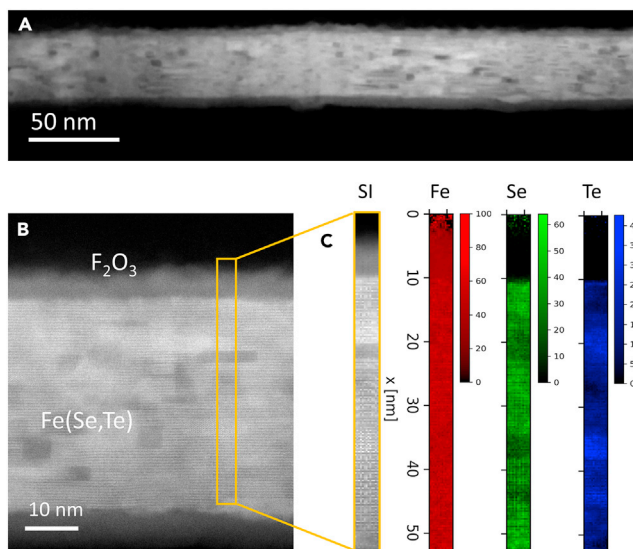
Figure 5. STEM images and EELS elemental maps of Fe(Se,Te) thin film
(A) Low-magnification STEM mass-contrast image.
(B) High-magnification STEM micrograph showing the region where spectrum imaging was performed.
(C) EELS elemental maps of Fe, Se, and Te in the spectrum imaging region.

Figure 7. We can infer that deviations from 3D G-L prediction of critical fields come out from microstructure in the Fe(Se,Te) case. The similar results obtained on YBCO material should instead be mainly ascribed to the layered structure itself and eventually 2D material defects commonly observed.[46] Our experimental findings demonstrate that such nanoscale microstructure in the Fe(Se,Te) can influence the behavior of critical field at 0.5 R_N, but it has no effect on the 0.9 R_N trend as expected.

In addition, a look up to $H_{irr}(\theta)$ in Figures 3 and 4 shows instead the marked difference between these two superconductors. In particular, for the Fe(Se,Te) compound, a highly isotropic pinning is expected due to the current transport in both directions parallel and perpendicular to the ab-plane,[42,44] whereas in YBCO an anisotropic trend is likely due to its intrinsic layered pinning exerted by the ab-planes. Our results are that Fe(Se,Te) shows backward a 3D behavior of $H_{irr}(\theta)$; on the contrary, YBCO still displays an even more accentuated 2D trend. All these findings support our proposal that pinning may affect the critical fields evaluated in different regions along the transition, so this becomes a warning and suggestion to disentangle intrinsic from extrinsic pinning effects by looking deeper into the H-θ phase diagram.

The results of combined angle-resolved electrical transport measurements with microstructure analysis offer, across all measurement techniques, a direct approach to investigate the superconductivity dimensionality and the material pinning anisotropy.

As a matter of fact, material dimensionality of any superconductor is determined by the upper critical field at 0.9 R_N. Our method guides into the structure and pinning influences along the superconducting transition.
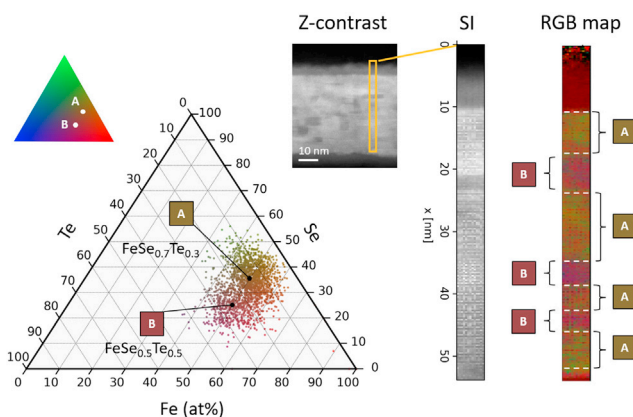

Figure 6. Ternary diagram showing the atomic percentage of Fe, Se, and Te within the region individuated by the SI and RGB map with colors coded according to points on ternary diagram
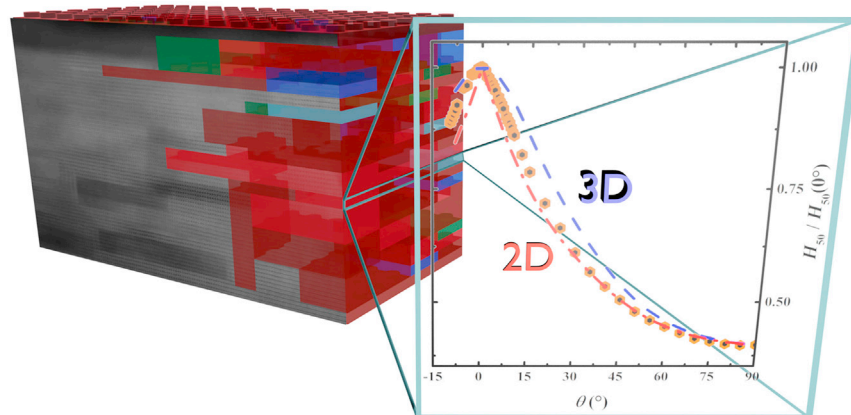
Figure 7. A sketch of the overall 2D grains-blocks growth in Fe(Se,Te) films that mimics a continuous layered structure of YBCO, resulting in a similar 2D anisotropic pinning behavior as proved by the $H_{50}(\theta)$ curve

Unlike 122-IBS family, in the Fe(Se,Te) 11-compound, a surprising anisotropy of $H_{c2}(\theta)$ is observed when the xR_N threshold was changed from 90% to 50%. We find a gradual evolution from a 3D to a 2D angular dependence reminding to a structural influence likewise in HTS materials. Indeed, this is what we observe in YBCO superconductor. Furthermore, the anisotropic parameter trend $\gamma(t)$ remarks this 3D-2D evolution with values going from below 2 up to 6, when changing from the 0.9 R_N threshold toward the 0.5 R_N for the Fe(Se,Te).

On top of that, we compare our experimental findings with a microstructure analysis very accurately performed on this Fe(Se,Te) superconductor, thus outlining a correspondence between the 2D growth-induced defects and the 2D behavior revealed in the H-θ phase diagram. This is totally confirmed by our results made for comparison on YBCO superconducting films, where the same trend from 3D toward 2D is explained by the presence of its intrinsic layered structure acting as the stronger pinning influence.

We conclude that layered structure and/or pinning effects can be revealed only through the H-θ measurements in different regions along the resistive transition. We have developed a general method for looking at the H-θ phase diagram that can be used as a guide for any other superconducting material. This overall study from the nanoscale imaging of material defects to the angular dependence of macroscopic properties presents a novel approach to discriminate in any other superconductor those fundamental properties, pinning dimensionality and material anisotropy 3D/2D at the same time, suitable for choosing a particular superconductor in view of a specific application.

STAR★METHODS

Detailed methods are provided in the online version of this paper and include the following:

- KEY RESOURCES TABLE
- RESOURCE AVAILABILITY
  - Lead contact
  - Materials availability
  - Data and code availability
- EXPERIMENTAL MODEL AND STUDY PARTICIPANT DETAILS
- METHOD DETAILS
- QUANTITATION AND STATISTICAL ANALYSIS
- ADDITIONAL RESOURCES

SUPPLEMENTAL INFORMATION

Supplemental information can be found online at https://doi.org/10.1016/j.isci.2024.109422.

ACKNOWLEDGMENTS

REFERENCES

1. Lei, H., Wang, K., Hu, R., Ryu, H., Abeykoon, M., Bozin, E.S., and Petrovic, C. (2012). Iron chalcogenide superconductors at high magnetic fields. Sci. Technol. Adv. Mater. 13, 054305. http://www.doi.org/10.1088/1468-6996/13/5/054305.

2. Oh, H., Moon, J., Shin, D., Moon, C.Y., and Choi, H.J. (2011). Brief review on iron-based superconductors: are there clues for unconventional superconductivity? Prog. Supercond. 13, 65–84. https://arxiv.org/abs/1201.0237.

3. Martucciello, N., Giubileo, F., Grimaldi, G., and Corato, V. (2015). Introduction to the focus on superconductivity for energy. Supercond. Sci. Technol. 28, 070201. http://www.doi.org/10.1088/0953-2048/28/7/070201.

4. Grimaldi, G., Leo, A., Nigro, A., Pace, S., Braccini, V., Bellingeri, E., and Ferdeghini, C. (2018). Angular dependence of vortex instability in a layered superconductor: the case study of Fe (Se, Te) material. Sci. Rep. 8, 4150–4159. http://www.doi.org/10.1038/s41598-018-22417-3.

5. Guarino, A., Leo, A., Grimaldi, G., Martucciello, N., Dean, C., Kunchur, M.N., Pace, S., and Nigro, A. (2014). Pinning mechanism in electron-doped HTS NdCeCuO epitaxial films. Supercond. Sci. Technol. 27, 124011. http://www.doi.org/10.1088/0953-2048/27/12/124011.

6. Grimaldi, G., Bauer, M., and Kinder, H. (2001). Continuous reel-to-reel measurement of critical currents of coated conductors. Appl. Phys. Lett. 79, 4390–4392. http://www.doi.org/10.1063/1.1428771.

7. Galluzzi, A., Buchkov, K., Nazarova, E., Tomov, V., Grimaldi, G., Leo, A., Pace, S., and Polichetti, M. (2019). Pinning energy and anisotropy properties of a Fe (Se, Te) iron-based superconductor. Nanotechnology 30, 254001. http://www.doi.org/10.1088/1361-6528/ab0c23.

8. Lei, H., Wang, K., Hu, R., Ryu, H., Abeykoon, M., Bozin, E.S., and Petrovic, C. (2012). Iron chalcogenide superconductors at high magnetic fields. Sci. Technol. Adv. Mater. 13, 054305. http://www.doi.org/10.1088/1468-6996/13/5/054305.

9. Pallecchi, I., Tropeano, M., Lamura, G., Pani, M., Palombo, M., Palenzona, A., and Putti, M. (2012). Upper critical fields and critical current densities of Fe-based superconductors as compared to those of other technical superconductors. Physica C (Amsterdam, Neth.) 482, 68–73. http://www.doi.org/10.1016/j.physc.2012.05.015.

10. Zhang, J.L., Jiao, L., Chen, Y., and Yuan, H.Q. (2011). Universal behavior of the upper critical field in iron-based superconductors. Front. Physiol. 6, 463–473. http://www.doi.org/10.1007/s11467-011-0235-7.

11. Llovo, I.F., Carballeira, C., Sóñora, D., Pereiro, A., Ponte, J.J., Salem-Sugui, S., Jr., Sefat, A.S., and Mosqueira, J. (2021). Multiband effects on the upper critical field angular dependence of 122-family iron pnictide superconductors. Sci. Rep. 11, 11526. http://www.doi.org/10.1038/s41598-021-90858-4.

12. Grissonnanche, G., Cyr-Choinière, O., Laliberté, F., René de Cotret, S., Juneau-Fecteau, A., Dufour-Beauséjour, S., Delage, M.È., LeBoeuf, D., Chang, J., Ramshaw, B.J., et al. (2014). Direct measurement of the upper critical field in cuprate superconductors. Nat. Commun. 5, 3280. http://www.doi.org/10.1038/ncomms4280.

13. Tanatar, M.A., Ishiguro, T., Tanaka, H., and Kobayashi, H. (2002). Magnetic field–temperature phase diagram of the quasi-two-dimensional organic superconductor λ−(BETS) 2 GaCl 4 studied via thermal conductivity. Phys. Rev. B 66, 134503. http://www.doi.org/10.1103/PhysRevB.66.134503.

14. Ma, K., Gornicka, K., Lefèvre, R., Yang, Y., Rønnow, H.M., Jeschke, H.O., Klimczuk, T., and Von Rohr, F.O. (2021). Superconductivity with high upper critical field in the cubic centrosymmetric η-carbide Nb4Rh2C1− δ. ACS Mater. Au 1, 55–61. http://www.doi.org/10.1021/acsmaterialsau.1c00011.

15. Borg, C.K.H., Zhou, X., Eckberg, C., Campbell, D.J., Saha, S.R., Paglione, J., and Rodriguez, E.E. (2016). Strong anisotropy in nearly ideal tetrahedral superconducting FeS single crystals. Phys. Rev. B 93, 094522. http://www.doi.org/10.1103/PhysRevB.93.094522.

16. Mizuguchi, Y., Yamada, A., Higashinaka, R., Matsuda, T.D., Aoki, Y., Miura, O., and Nagao, M. (2016). Specific heat and electrical transport properties of Sn0. 8Ag0. 2Te superconductor. J. Phys. Soc. Jpn. 85, 103701. http://www.doi.org/10.7566/JPSJ.85.103701.

17. Mizuguchi, Y., Takeya, H., Kawasaki, Y., Ozaki, T., Tsuda, S., Yamaguchi, T., and Takano, Y. (2011). Transport properties of the new Fe-based superconductor KxFe2Se2 (Tc= 33 K). Appl. Phys. Lett. 98. http://www.doi.org/10.1063/1.3549702.

18. Li, C.H., Shen, B., Han, F., Zhu, X., and Wen, H.H. (2011). Transport properties and anisotropy of Rb 1− x Fe 2− y Se 2 single crystals. Phys. Rev. B 83, 184521. http://www.doi.org/10.1103/PhysRevB.83.184521.

19. Leo, A., Guarino, A., Grimaldi, G., Nigro, A., Pace, S., Bellingeri, E., Kawale, S., Ferdeghini, C., and Giannini, E. (2014). Comparison of the pinning energy in Fe (Se1− xTex) compound between single crystals and thin films. In Journal of Physics: Conference Series, 507Journal of Physics: Conference Series (IOP Publishing), p. 012029. http://www.doi.org/10.1088/1742-6596/507/1/012029.

20. Leo, A., Grimaldi, G., Marra, P., Citro, R., Avitabile, F., Guarino, A., Bellingeri, E., Kawale, S., Ferdeghini, C., Nigro, A., and Pace, S. (2016). Stability mechanisms of high current transport in iron-chalcogenide superconducting films. IEEE Trans. Appl. Supercond. 26, 1–4. http://www.doi.org/10.1109/TASC.2016.2542247.

21. Leo, A., Sylva, G., Braccini, V., Bellingeri, E., Martinelli, A., Pallecchi, I., Ferdeghini, C., Pellegrino, L., Putti, M., Ghigo, G., et al. (2019). Anisotropic effect of proton irradiation on pinning properties of Fe (Se, Te) thin films. IEEE Trans. Appl. Supercond. 29, 1–5. http://www.doi.org/10.1109/TASC.2019.2893592.

22. Galluzzi, A., Buchkov, K., Tomov, V., Nazarova, E., Kovacheva, D., Leo, A., Grimaldi, G., Pace, S., and Polichetti, M. (2018). Mixed state properties of iron-based Fe (Se, Te) superconductor fabricated by Bridgman and by self-flux methods. J. Appl. Phys. 123, 233904. http://www.doi.org/10.1063/1.5032202.

23. Kida, T., Matsunaga, T., Hagiwara, M., Mizuguchi, Y., Takano, Y., and Kindo, K. (2009). Upper critical fields of the 11-system iron-chalcogenide superconductor FeSe0. 25Te0. 75. J. Phys. Soc. Jpn. 78, 113701. http://www.doi.org/10.1143/JPSJ.78.113701.

24. Murphy, J., Tanatar, M.A., Graf, D., Brooks, J.S., Bud'Ko, S.L., Canfield, P.C., Kogan, V.G., and Prozorov, R. (2013). Angular-dependent upper critical field of overdoped Ba (Fe 1− x Ni x) 2 As 2. Phys. Rev. B 87, 094505. http://www.doi.org/10.1103/PhysRevB.87.094505.

25. Krasnov, V.M., Kovalev, A.E., Oboznov, V.A., and Pedersen, N.F. (1996). Magnetic field

decoupling and 3D-2D crossover in Nb/Cu multilayers. Phys. Rev. B *54*, 15448–15456. http://www.doi.org/10.1103/PhysRevB.54.15448.

26. Attanasio, C., Coccorese, C., Mercaldo, L.V., Salvato, M., Maritato, L., Lykov, A.N., Prischepa, S.L., and Falco, C.M. (1998). Angular dependence of the upper critical field in Nb/CuMn multilayers. Phys. Rev. B *57*, 6056–6060. http://www.doi.org/10.1103/PhysRevB.57.6056.

27. Skocpol, W.J., and Tinkham, M. (1975). Fluctuations near superconducting phase transitions. Rep. Prog. Phys. *38*, 1049–1097. http://www.doi.org/10.1088/0034-4885/38/9/001.

28. Marra, P., Nigro, A., Li, Z., Chen, G.F., Wang, N.L., Luo, J.L., and Noce, C. (2012). Paraconductivity of the K-doped SrFe2As2 superconductor. New J. Phys. *14*, 043001. http://www.doi.org/10.1088/1367-2630/14/4/043001.

29. Bellingeri, E., Pallecchi, I., Buzio, R., Gerbi, A., Marrè, D., Cimberle, M.R., Tropeano, M., Putti, M., Palenzona, A., and Ferdeghini, C. (2010). Tc= 21 K in epitaxial FeSe$_{0.5}$Te$_{0.5}$ thin films with biaxial compressive strain. Appl. Phys. Lett. *96*, 102512. https://www.doi.org/10.1063/1.3358148.

30. Kawale, S., Bellingeri, E., Braccini, V., Pallecchi, I., Putti, M., Grimaldi, G., Leo, A., Guarino, A., Nigro, A., and Ferdeghini, C. (2012). Comparison of superconducting properties of FeSe0.5Te0.5 thin films grown on different substrates. IEEE Trans. Appl. Supercond. *23*, 7500704. http://www.doi.org/10.1109/TASC.2012.2235899.

31. Augieri, A., Celentano, G., Galluzzi, V., Mancini, A., Rufoloni, A., Vannozzi, A., Armenio, A.A., Petrisor, T., Ciontea, L., Rubanov, S., et al. (2010). Pinning analyses on epitaxial YBa2Cu3O7− δ films with BaZrO3 inclusions. J. Appl. Phys. *108*, 063906. https://www.doi.org/10.1063/1.3477451.

32. Grimaldi, G., Leo, A., Avitabile, F., Martucciello, N., Galluzzi, A., Polichetti, M., Pace, S., and Nigro, A. (2019). Vortex lattice instability at the nanoscale in a parallel magnetic field. Nanotechnology *30*, 424001. http://www.doi.org/10.1088/1361-6528/ab3314.

33. Abdel-Hafiez, M., Zhao, X.M., Kordyuk, A.A., Fang, Y.W., Pan, B., He, Z., Duan, C.G., Zhao, J., and Chen, X.J. (2016). Enhancement of superconductivity under pressure and the magnetic phase diagram of tantalum disulfide single crystals. Sci. Rep. *6*, 31824. http://www.doi.org/10.1038/srep31824.

34. Bellingeri, E., Kawale, S., Caglieris, F., Braccini, V., Lamura, G., Pellegrino, L., Sala, A., Putti, M., Ferdeghini, C., Jost, A., et al. (2014). High field vortex phase diagram of Fe (Se, Te) thin films. Supercond. Sci. Technol. *27*, 044007. http://www.doi.org/10.1088/0953-2048/27/4/044007.

35. Fiamozzi Zignani, C., De Marzi, G., Corato, V., Mancini, A., Vannozzi, A., Rufoloni, A., Leo, A., Guarino, A., Galluzzi, A., Nigro, A., et al. (2019). Improvements of high field pinning properties of polycrystalline Fe (Se, Te) material by heat treatments. J. Mater. Sci. *54*, 5092–5100. http://www.doi.org/10.1007/s10853-018-03218-5.

36. Lu, J.M., Zheliuk, O., Leermakers, I., Yuan, N.F.Q., Zeitler, U., Law, K.T., and Ye, J.T. (2015). Evidence for two-dimensional Ising superconductivity in gated MoS2. Science *350*, 1353–1357. http://www.doi.org/10.1126/science.aab2277.

37. Banerjee, I., Yang, Q.S., Falco, C.M., and Schuller, I.K. (1983). Anisotropic critical fields in superconducting superlattices. Phys. Rev. B *28*, 5037–5040. http://www.doi.org/10.1103/PhysRevB.28.5037.

38. Tinkham, M. (1963). Effect of fluxoid quantization on transitions of superconducting films. Phys. Rev. *129*, 2413–2422. http://www.doi.org/10.1103/physrev.29.2413.

39. Tinkham, M. (2004). Introduction to Superconductivity (Courier Corporation).

40. Naughton, M.J., Yu, R.C., Davies, P.K., Fischer, J.E., Chamberlin, R.V., Wang, Z.Z., Jing, T.W., Ong, N.P., and Chaikin, P.M. (1988). Orientational anisotropy of the upper critical field in single-crystal Y Ba 2 Cu 3 O 7 and Bi 2.2 Ca Sr 1.9 Cu 2 O 8+ x. Phys. Rev. B *38*, 9280–9283. http://www.doi.org/10.1103/physrevb.38.9280.

41. Yuan, H.Q., Singleton, J., Balakirev, F.F., Baily, S.A., Chen, G.F., Luo, J.L., and Wang, N.L. (2009). Nearly isotropic superconductivity in (Ba, K) Fe2As2. Nature *457*, 565–568. http://www.doi.org/10.1038/nature07676.

42. Scuderi, M., Pallecchi, I., Leo, A., Nigro, A., Grimaldi, G., Ferdeghini, C., Spinella, C., Guidolin, M., Trotta, A., and Braccini, V. (2021). Nanoscale analysis of superconducting Fe(Se,Te) epitaxial thin films and relationship with pinning properties. Sci. Rep. *11*, 20100. http://www.doi.org/10.1038/s41598-021-99574-5.

43. Khan, M.R., Leo, A., Nigro, A., Galluzzi, A., Polichetti, M., Braccini, V., Cialone, M., Scuderi, M., and Grimaldi, G. (2021). Effective Magnetic Field Dependence of the Flux Pinning Energy in FeSe0. 5Te0. 5 Superconductor. Materials *14*, 5289. http://www.doi.org/10.3390/ma14185289.

44. Braccini, V., Kawale, S., Reich, E., Bellingeri, E., Pellegrino, L., Sala, A., Putti, M., Higashikawa, K., Kiss, T., Holzapfel, B., and Ferdeghini, C. (2013). Highly effective and isotropic pinning in epitaxial Fe (Se, Te) thin films grown on CaF2 substrates. Appl. Phys. Lett. *103*, 172601. https://www.doi.org/10.1063/1.4826677.

45. Sun, Q., Xu, Z., Dong, C., Huang, H., Wang, D., Zhang, X., and Ma, Y. (2023). Macroscopically ordered phase separation: A new strategy for improving the superconducting performance in Fe (Se, Te). Mater. Today Adv. *17*, 100354. http://www.doi.org/10.1016/j.mtadv.2023.100354.

46. Palau, A., Vallès, F., Rouco, V., Coll, M., Li, Z., Pop, C., Mundet, B., Gàzquez, J., Guzman, R., Gutierrez, J., et al. (2018). Disentangling vortex pinning landscape in chemical solution deposited superconducting YBa2Cu3O7− x films and nanocomposites. Supercond. Sci. Technol. *31*, 034004. http://www.doi.org/10.1088/1361-6668/aaa65e.

STAR★METHODS

KEY RESOURCES TABLE

REAGENT or RESOURCE	SOURCE	IDENTIFIER
Software and algorithms		
OriginPro 2023 Build No. 10.0.0.154	OriginLab	https://www.originlab.com/index.aspx?go=Products/Origin

RESOURCE AVAILABILITY

Lead contact

Further information and requests for resources and reagents should be directed to and will be fulfilled by the lead contact, Gaia Grimaldi (gaia.grimaldi@spin.cnr.it).

Materials availability

This study did not generate new unique reagents.

Data and code availability

- Data reported in this paper will be shared by the lead contact upon request.
- This paper does not report original codes.
- Any additional information required to reanalyze the data reported in this paper is available from the lead contact upon request.

EXPERIMENTAL MODEL AND STUDY PARTICIPANT DETAILS

The OriginPro software has been employed to analyze data estimating critical parameters values and model curves based on common definitions given in the main text.

METHOD DETAILS

Critical field values have been estimated from magneto-resistance measurement data as explained in the main text and as shown in Figure 1. Critical current density values have been evaluated from current-voltage measurements setting as a threshold 1 μV. 3D GL and 2D Tinkham model curves have been generated by using equation given in the main text, using for $H_{c2}^{\parallel}$ and $H_{c2}^{\perp}$ the H_{max} and H_{min} values from Tables 1 and 2, respectively.

QUANTITATION AND STATISTICAL ANALYSIS

Model curves have been generated by OriginPro software. Figures shown in this work have been produced by OriginPro, Blender, and Microsoft Powerpoint softwares.

ADDITIONAL RESOURCES

Any additional information about the simulation and data reported in this paper is available from the lead contact on request.